A multiscale model for the elastoviscoplastic behavior of Directionally Solidified alloys: Application to FE structural computations

Guillaume Martin, N. Ochoa, Kacem Sai, Eveline Hervé-Luanco, Georges Cailletaud

International Journal of Solids and Structures 51 (2014) 1175–1187

Contents lists available at ScienceDirect

International Journal of Solids and Structures

journal homepage: www.elsevier.com/locate/ijsolstr

A multiscale model for the elastoviscoplastic behavior of Directionally Solidified alloys: Application to FE structural computations

G. Martin [a,d], N. Ochoa [a], K. Saï [b,*], E. Hervé-Luanco [c], G. Cailletaud [a]

[a] MINES ParisTech, Centre des Matériaux, CNRS UMR7633, BP 87, 91003 Evry Cedex, France
[b] UGPMM, Ecole Nationale d'Ingénieurs de Sfax, BP 1173 Sfax, Tunisia
[c] Université de Versailles St-Quentin-en-Yvelines, 45 rue des Etats-Unis, 78035 Versailles Cedex, France
[d] Snecma Villaroche, Rond-point René Ravaud, Réau 77550, Moissy-Cramayel, France

ARTICLE INFO

Article history:
Received 21 April 2013
Received in revised form 6 December 2013
Available online 14 December 2013

Keywords:
Directionally Solidified alloy
Homogenization
Mean field model
Finite Element analysis

ABSTRACT

A mean field mechanical model describing the inelastic behavior and strong anisotropy of Directionally Solidified (DS) materials is developed. Its material parameters are calibrated by comparison with the Finite Element (FE) computation of a Representative Volume Element (RVE). In the case of a large grain alloy where microstructure size cannot be neglected with respect to geometrical variations, this approach is a good candidate to evaluate the local scatter coming from the material heterogeneity.

1. Introduction

Aeronautical and space industries show a growing interest for Directionally Solidified (DS) materials, especially for nickel-based superalloys. These alloys are used in components operating at high temperatures like turbine blades (Vladimirov et al., 2009; Yang et al., 2011; Shi et al., 2012; Chen et al., 2012). This kind of structure is a good compromise between high resistance–high cost single crystal and cheaper polycrystalline materials: DS alloys manufacturing is easier than single crystal, and it presents higher mechanical properties than polycrystals for a large range of temperature. In DS microstructures, grains have a purely columnar morphology, the $\langle 001 \rangle$ direction being the same for all of them (x_3 direction in this paper), and the secondary orientation having a random character in the normal plane, Fig. 1(a). DS like microstructures are also present in other components like combustion chambers, for which the solidification process generates preferentially oriented columnar grains perpendicular to the surface in thin wall zones. Such parts classically show heterogeneous microstructures, where the columnar grains, present in a limited area, are surrounded by large zones made of small equiaxed grains.

Both grain morphology and crystal orientation produce a strong anisotropy that is a crucial matter for component design. This effect is more and more sensitive when the grain size remains large with respect to the geometry of the component. A variation can then be observed from one component to the other, so that the estimation of the time to failure should include a statistical approach. The evaluation of the stress distribution can be achieved on a series of realizations, using an explicit modeling of the grains in the component, and a full-field approach where the orientation distribution comes from experimental Electron BackScatter Diffraction (EBSD) measurements. However, this time-consuming method is not appropriate for industrial applications. In this framework, results obtained with mean-field models are analyzed, in order to check if a one-shot computation with a DS model is able to reproduce a series of calculations with various geometrical and crystallographic realizations. Mean field approach has already been used in the literature to predict the mechanical behavior of DS microstructures: elastic anisotropy has been investigated by Hasebe et al. (1992), Hendrix and Yu (1998), and Yaguchi and Busso (2005), using Kneer's self-consistent elastic scheme (Kneer, 1965), while inelastic evolution has yet been predicted in the work of Saï et al. (2006), by means of an adapted Kröner's self-consistent approach (Kröner, 1961) with a uniform elastic local behavior. However, to authors' best knowledge, there is no attempt to account for both elastic and inelastic heterogeneities in such materials.

In the two last decades, DS materials have been the subject of a growing interest inducing an intense experimental activity and theoretical developments (Kowalewski and Mughrabi, 1998; Okada et al., 1998; Yuan et al., 1998; Wang et al., 2006; Gordon et al., 2007; Xia et al., 2008; Zhao et al., 2008; Nie et al., 2009; Chu et al., 2010; Latief et al., 2014). The creep behavior of DS

* Corresponding author. Tel.: +216 74 274 088; fax: +216 74 275 59.
E-mail address: kacemsai@yahoo.fr (K. Saï).

0020-7683/$ - see front matter © 2013 Elsevier Ltd. All rights reserved.
http://dx.doi.org/10.1016/j.ijsolstr.2013.12.013

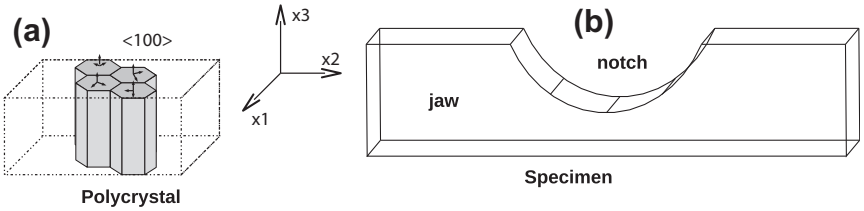

Fig. 1. (a) Columnar morphology of DS grains. (b) Notched specimen used to evaluate the various models.

Nickel-base superalloy GTD 111 has been investigated at various temperatures (649–982 °C) and stresses (124 MPa to 896 MPa) by Ibanez et al. (2006). Other researchers (Kupkovits and Neu, 2010) performed cyclic tests on smooth and notched CM247LC specimens, with longitudinal or transverse grain orientation. The thermomecanical loading is applied either in-phase or out-of-phase. The deformation and damage mechanisms are linked to the severity of the notch and the temperature history. The model framework is crystal plasticity, in order to highlight the effect of the elastic modulus and to link fatigue life to both temperature and the microstructure. The same material has been characterized in low cycle fatigue at 750 °C and 950 °C, using various strain rates, dwells at the maximum temperature, and stress concentrations (Moore and Neu, 2011). Low cycle fatigue and creep-fatigue tests of a DS like Nickel-base superalloy (DZ112) have been performed by Shi et al. (2010) at 850 °C in order to study the influence of dwell time on creep-fatigue interaction. Macroscopic elastoviscoplastic models coupled with anisotropy and/or damage have been developed to capture the fatigue and creep behavior of DS Nickel-base superalloys (Österle et al., 2000; Han et al., 2001a,b; Prasad et al., 2005, 2006; Shenoy et al., 2006; Ibanez et al., 2006; Yaguchi et al., 2007; Moore and Neu, 2011; Stewart et al., 2011; Shi et al., 2013). An other group of studies deals with the integrity of DS materials. The fluctuation of J-integral, during high-temperature fatigue crack propagation, due to the microscopic inclination of crack and the elastic anisotropy of each grain has been investigated by means of a series of FE analysis on a cracked body made of DS Nickel-base superalloy (Yamamoto et al., 2008). Cyclic fatigue assessment has been performed using a modified Hill approach to describe the anisotropic failure surface (Bernhardi and Mücke, 2000). The effect of pre-exposure to the oxide spiking damage mechanism and crack initiation life has been characterized for a DS Nickel-base superalloy (GTD-111) by Gordon et al. (2009).

The present work aims at describing the effects of elastic and inelastic heterogenetities in the Nickel-base superalloy Inconel 718, using the multiscale scheme proposed by Sabar et al. (2002). It is demonstrated that elasticity and plasticity have their own contributions to anisotropy that must be taken into account. Their respective effects are calibrated by means of FE computations, and included into the mean-field model. The latter is then used to predict the scatter of the stress field in a notched component, Fig. 1(b), where the two jaws are made of equiaxed grains while the notch is composed of DS grains, the solidification direction being normal to the free surface.

The paper is organized in the following manner. The various transition rules used for the mean-field computations and the constitutive equations which are based on crystal plasticity are presented in Section 2. In Section 3, the material parameters defining the single crystal behavior are obtained following a precise identification strategy. These parameters are then applied to DS grains, in order to exhibit the anisotropic behavior of the microstructure. In Section 4, a FE analysis of an Inconel 718 notched specimen is performed with three approaches: use of a macroscopic model; explicit full field description of the material (e.g., the various grains) in the component; computation with the mean-field model.

2. Multiscale schemes applied to polycrystalline aggregates

A self-consistent approach of the polycrystal modeling has been developed by Hill (1965) for elastoplastic material. The model is briefly recalled in this section, together with simplified expressions in the case of uniform elasticity. The case of elastoviscoplastic behavior will be considered as well, by means of a translated fields approach.

2.1. Hill's model

In the model, a "phase" represents all the grains that are in a given class of crystallographic orientation. An average stress and strain is attributed to this phase, that will still be denoted by the word "grain" in the following. The global behavior results from the resolution of a series of auxiliary problems that assumes each grain g behaves like an ellipsoidal inclusion embedded in a homogeneous effective medium (HEM) resulting from the average of all the grains. Eshelby's inclusion formalism (Eshelby, 1957) is used to describe the interaction between each grain and the aggregate. In this classical theory, the stress state in the inclusion results from an eigenstrain $\underset{\sim}{\varepsilon}^L$. The HEM surrounding the inclusion undergoes, at infinity, an eigenstrain $\underset{\sim}{E}^L$ when the overall strain $\underset{\sim}{E}$ is applied.

A rate form must be applied for the case of elastoplasticity. This is why a linearization procedure is introduced by Hill (1965), leading to the following elasto-plastic instantaneous moduli:

$$\dot{\underset{\sim}{\sigma}}_g = \underset{\approx}{L}_g : \dot{\underset{\sim}{\varepsilon}}_g \tag{1}$$

$$\dot{\underset{\sim}{\Sigma}} = \underset{\approx}{L}^{eff} : \dot{\underset{\sim}{E}} \tag{2}$$

Solving Eshelby's problem provides the strain and stress rates at the grain level:

$$\dot{\underset{\sim}{\varepsilon}}_g = \dot{\underset{\sim}{E}} + \underset{\approx}{S} : \dot{\underset{\sim}{\varepsilon}}^L \tag{3}$$

$$\dot{\underset{\sim}{\sigma}}_g = \underset{\approx}{L}^{eff} : \left(\dot{\underset{\sim}{\varepsilon}}_g - \dot{\underset{\sim}{\varepsilon}}^L\right) \tag{4}$$

where $\underset{\approx}{S}$ is the well known Eshelby's tensor. This four-rank tensor is linked to the elastic tensor of the HEM $\underset{\approx}{C}^{eff}$ and the inclusion morphology.

From these equations, relations between local and overall states can be defined introducing a transition rule, Eq. (5), and strain rate concentration tensors $\underset{\approx}{A}_g$, Eq. (6):

$$\dot{\underset{\sim}{\sigma}}_g = \dot{\underset{\sim}{\Sigma}} + \underset{\approx}{L}^{\star} : \left(\dot{\underset{\sim}{E}} - \dot{\underset{\sim}{\varepsilon}}_g\right) \quad \text{with } \underset{\approx}{L}^{\star} = \underset{\approx}{L}^{eff} : \left(\underset{\approx}{S}^{-1} - \underset{\approx}{I}\right) \tag{5}$$

$$\dot{\underset{\sim}{\varepsilon}}_g = \underset{\approx}{A}_g : \dot{\underset{\sim}{E}} \quad \text{with } \underset{\approx}{A}_g = \left[\underset{\approx}{I} - \underset{\approx}{S} : \left(\underset{\approx}{I} - \underset{\approx}{L}^{eff^{-1}} : \underset{\approx}{L}_g\right)\right]^{-1} \tag{6}$$

where $\underset{\approx}{I}$ is the fourth-rank identity tensor, and $\underset{\approx}{L}^{\star}$ is the accommodation tensor. Thus, effective tangent operator has an implicit form:

$$\underset{\approx}{L}^{eff} = \left\langle \underset{\approx}{L}_g : \underset{\approx}{A}_g \right\rangle \tag{7}$$

Depending on the microstructure, the model can be derived into different forms:

- For an equiaxed microstructure, Eshelby's inclusions can be considered as spherical (Fig. 2). The local elasticity $\underset{\approx}{C}_g$, according to the *fcc* (face centered cubic) crystal structure of Nickel-base alloys, has a cubic symmetry, Eq. (B.1). If homogenization is applied on a large number of randomly oriented grains, HEM elasticity becomes isotropic ($\underset{\approx}{C}^{eff}=\underset{\approx}{\Lambda}^{eff}$). In this particular case, Eshelby's tensor depends only on Poisson's ratio ν, Eq. (B.4).
- For DS microstructures, the columnar geometry can be represented by a collection of infinite cylinders (Fig. 3) along x_3 ($a_1 = a_2, a_3 \to \infty$), so that the Eshelby's tensor takes the form:

$$\underset{\approx}{S} = \begin{pmatrix} S_{1111} & S_{1122} & S_{1133} & 0 & 0 & 0 \\ S_{1122} & S_{1111} & S_{1133} & 0 & 0 & 0 \\ 0 & 0 & 0 & 0 & 0 & 0 \\ 0 & 0 & 0 & S_{2323} & 0 & 0 \\ 0 & 0 & 0 & 0 & S_{2323} & 0 \\ 0 & 0 & 0 & 0 & 0 & S_{1212} \end{pmatrix} \tag{8}$$

It results from Eq. (3) that $\varepsilon_{g33} = E_{33}$. If the polycrystal contains a sufficient number of DS grains, the elasticity tensor presents a transverse isotropy, Eq. (B.2). Starting from the cubic elasticity tensor, C^0 the elasticity tensor of any randomly oriented DS single crystal can be expressed as follows:

$$\underset{\approx}{C}_g = \left(\underset{\sim}{R}_\theta \underline{\otimes} \underset{\sim}{R}_\theta\right) : \underset{\approx}{C}^0 : \left(\underset{\sim}{R}_\theta \underline{\otimes} \underset{\sim}{R}_\theta\right)^T \tag{9}$$

where $\underset{\sim}{R}_\theta$ characterizes a rotation θ around x_3 axis.

2.2. Simplified schemes

The model can be simplified if the elasticity is assumed to be uniform in the polycrystal ($\underset{\approx}{C}_g = \underset{\approx}{C}^{eff}$). In this case the heterogeneities relates to plastic behavior only, and Hill's transition rule can be turned to:

$$\underset{\sim}{\sigma}_g = \underset{\sim}{\Sigma} + \underset{\approx}{L}^\star : \left[\underset{\approx}{C}^{eff^{-1}} : \left(\underset{\sim}{\Sigma} - \underset{\sim}{\sigma}_g\right) + \left(\underset{\sim}{E}^p - \underset{\sim}{\varepsilon}^p_g\right)\right]$$

$$\underset{\sim}{\sigma}_g = \underset{\sim}{\Sigma} + \left(\underset{\approx}{I} + \underset{\approx}{L}^\star : \underset{\approx}{C}^{eff^{-1}}\right)^{-1} : \underset{\approx}{L}^\star : \left(\underset{\sim}{E}^p - \underset{\sim}{\varepsilon}^p_g\right) \tag{10}$$

Equiaxed microstructures and DS materials lead then to different expressions, as shown below.

2.2.1. Equiaxed microstructure

For the description of particular symmetries, two four-rank tensors namely $\underset{\approx}{K}$ and $\underset{\approx}{J}$ are introduced. $\underset{\approx}{K}$ and $\underset{\approx}{J}$ transform any second-order tensor $\underset{\sim}{a}$ to its spherical and deviatoric part, respectively.

$$\underset{\approx}{K} : \underset{\sim}{a} = \frac{1}{3} Tr(\underset{\sim}{a})\, \underset{\sim}{I} \tag{11}$$

$$\underset{\approx}{J} : \underset{\sim}{a} = dev(\underset{\sim}{a}) = \underset{\sim}{a} - \underset{\approx}{K} : \underset{\sim}{a} \tag{12}$$

It is worth noting that:

$$\underset{\approx}{K} + \underset{\approx}{J} = \underset{\approx}{I}, \quad \underset{\approx}{K} : \underset{\approx}{J} = \underset{\approx}{J} : \underset{\approx}{K} = \underset{\approx}{0}, \quad \underset{\approx}{K} : \underset{\approx}{K} = \underset{\approx}{K} \quad \text{and} \quad \underset{\approx}{J} : \underset{\approx}{J} = \underset{\approx}{J} \tag{13}$$

As mentioned before (Fig. 2), the elasticity tensor of a polycrystal composed of equiaxed grains has an isotropic symmetry, thus:

$$\underset{\approx}{\Lambda}^{eff} = 3k \underset{\approx}{K} + 2\mu \underset{\approx}{J} \tag{14}$$

where μ and k are respectively the shear and the bulk modulus. They can be expressed as functions of E and ν:

$$\mu = \frac{E}{2(1+\nu)} \quad \text{and} \quad k = \frac{E}{3(1-2\nu)} \tag{15}$$

In the same way, the Eshelby's tensor representing a spherical inclusion in an isotropic HEM can be decomposed:

$$\underset{\approx}{S} = \alpha \underset{\approx}{K} + \beta \underset{\approx}{J} \tag{16}$$

with

$$\alpha = \frac{3k}{3k+4\mu} \quad \text{and} \quad \beta = \frac{6(k+2\mu)}{5(3k+4\mu)} \tag{17}$$

Berveiller and Zaoui (1979) have proposed an isotropic approximation of the effective secant operator, introducing an approximate isotropic moduli such that:

$$\underset{\approx}{L}^{eff} = 3k' \underset{\approx}{K} + 2\mu' \underset{\approx}{J} \tag{18}$$

Eq. (10) can then be simplified, and by considering that local and global plastic strain traces are zero, the so called Berveiller–Zaoui transition rule is obtained:

$$\underset{\sim}{\sigma}_g = \underset{\sim}{\Sigma} + 2\mu \frac{(1-\beta)\mu'}{\beta\mu + (1-\beta)\mu'} \left(\underset{\sim}{E}^p - \underset{\sim}{\varepsilon}^p_g\right) \tag{19}$$

Finally, this expression reduces to:

$$\underset{\sim}{\sigma}_g = \underset{\sim}{\Sigma} + 2\mu(1-\beta)\alpha\left(\underset{\sim}{E}^p - \underset{\sim}{\varepsilon}^p_g\right) \quad \text{with} \quad \frac{1}{\alpha} = 1 + \frac{3}{2}\frac{\|\underset{\sim}{E}^p\|}{J(\underset{\sim}{\Sigma})} \tag{20}$$

where $J(\underset{\sim}{\Sigma})$ and $\|\underset{\sim}{E}^p\|$ are the equivalent von Mises overall stress and the equivalent overall plastic strain, respectively.

2.2.2. DS microstructure

Without accounting for plasticity in the HEM ($\underset{\approx}{L}^{eff} = \underset{\approx}{C}^{eff}$), the following rule had been proposed by Kröner (1961):

$$\underset{\sim}{\sigma}_g = \underset{\sim}{\Sigma} + \underset{\approx}{C}^{eff} : \left(\underset{\approx}{I} - \underset{\approx}{S}\right) : \left(\underset{\sim}{E}^p - \underset{\sim}{\varepsilon}^p_g\right) \tag{21}$$

Since elasticity replaces plasticity in the HEM, the resulting behavior is then too hard, since the internal stresses are overestimated. Compared with Hill's model, the nonlinearity of the operator multiplying the difference between global and local plastic strain tensors is not introduced. Nevertheless, this model can be taken as a new starting point for an alternative approach, where the nonlinearity is transferred to the term that represents heterogeneity. This is made in the so called β-rule that introduces a state accommodation variable $\underset{\sim}{\beta}_g$ with a non linear evolution (Cailletaud, 1992; Pilvin, 1994; Cailletaud and Saï, 2008):

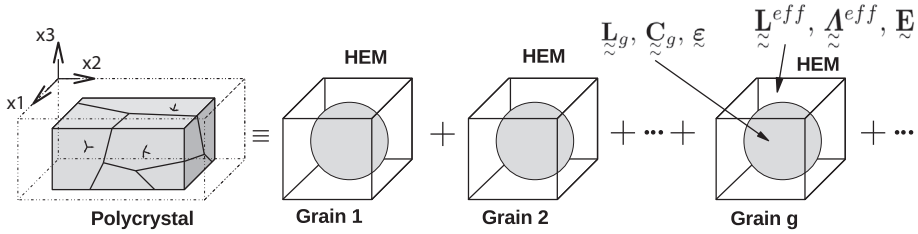

Fig. 2. Eshelby's problem for equiaxed microstructures.

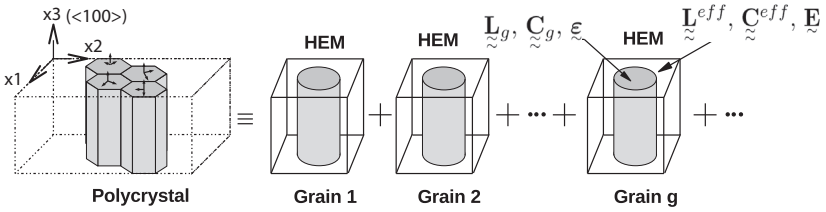

Fig. 3. Eshelby's problem for DS microstructures.

$$\dot{\underset{\sim}{\beta}}_g = \dot{\underset{\sim}{\varepsilon}}^p_g - \underset{\approx}{D} : \underset{\sim}{\beta}_g \|\dot{\underset{\sim}{\varepsilon}}^p_g\| \tag{22}$$

The concept has been specialized to DS alloys by Saï et al. (2006), according to:

$$\underset{\sim}{\sigma}_g = \underset{\sim}{\Sigma} + \underset{\approx}{\Lambda}^{eff} : \left(\underset{\approx}{I} - \underset{\approx}{S}\right) : \left(\underset{\sim}{\beta} - \underset{\sim}{\beta}_g\right) \quad \text{with} \quad \underset{\sim}{\beta} = \left\langle \underset{\sim}{\beta}_g \right\rangle \tag{23}$$

The tensor $\underset{\approx}{D}$ involves five independent material parameters shown in Table 1. They have been fitted by comparison to tensile test simulations obtained with (i) the mean-field model, Eq. (23) (ii) by averaging the full-field FE responses of a RVE of DS material.

2.3. Translated fields

The previous models are valid for time independent elastoplasticity. An alternative framework should be chosen to account for viscoplastic flow. The scheme proposed by Sabar et al. (2002), which is based on the integral equation for a translated strain rate field is a good candidate, that introduces an independent treatment of the instantaneous elastic fields and time-dependent viscoplastic ones:

$$\underset{\sim}{\sigma}_g = \underset{\approx}{C}_g : \underset{\sim}{\varepsilon}^e_g = \underset{\approx}{B}_g : \dot{\underset{\sim}{\varepsilon}}^p_g \tag{24}$$

$$\underset{\sim}{\Sigma} = \underset{\approx}{C}^{eff} : \underset{\sim}{E}^e = \underset{\approx}{B}^{eff} : \dot{\underset{\sim}{E}}^p \tag{25}$$

where $\underset{\approx}{B}_g$ and $\underset{\approx}{B}^{eff}$ are respectively the local and effective secant viscoplastic moduli. Introducing fluctuation terms in the moduli ($\underset{\approx}{C}_g = \underset{\approx}{C} + \delta\underset{\approx}{c}_g, \underset{\approx}{B}_g = \underset{\approx}{B} + \delta\underset{\approx}{b}_g$), gives the opportunity to write strain rate concentration tensors for each part of the deformation ($\underset{\approx}{A}^C_g, \underset{\approx}{A}^B_g$), such as:

$$\dot{\underset{\sim}{\varepsilon}}^e_g = \underset{\approx}{A}^C_g : \dot{\underset{\sim}{E}}^e \quad \text{with } \underset{\approx}{A}^C_g = \left[\underset{\approx}{I} + \underset{\approx}{S} : \underset{\approx}{C}^{eff^{-1}} : \delta\underset{\approx}{c}_g\right]^{-1} \tag{26}$$

$$\dot{\underset{\sim}{\varepsilon}}^p_g = \underset{\approx}{A}^B_g : \dot{\underset{\sim}{E}}^p \quad \text{with } \underset{\approx}{A}^B_g = \left[\underset{\approx}{I} + \underset{\approx}{T} : \underset{\approx}{B}^{eff^{-1}} : \delta\underset{\approx}{b}_g\right]^{-1} \tag{27}$$

where T is the equivalent Eshelby's tensor for the secant operator B. Unlike elasticity tensor, this viscoplastic operator has to be considered with the general orthotropic symmetry. In this case, general Eshelby's equation has to be applied, as defined in Mura (1987), using a numerical integration (see Appendix C). Self-consistency leads to:

$$\underset{\approx}{C}^{eff} = \left\langle \underset{\approx}{C}_g : \underset{\approx}{A}^C_g \right\rangle, \quad \underset{\approx}{B}^{eff} = \left\langle \underset{\approx}{B}_g : \underset{\approx}{A}^B_g \right\rangle \tag{28}$$

According to Sabar et al. (2002), the combination of both elastic and viscoplastic parts gives:

Table 1
D_{ijkl} constant values fitted for DS microstructures ($D_{3333} = D_{1111} + D_{1122} - D_{2233}, D_{2222} = D_{1111}, D_{1133} = D_{2233}, D_{3131} = D_{2323}$, other components are zero).

D_{1111}	D_{2233}	D_{1122}	D_{1212}	D_{2323}
1000	100	75	10	100

$$\dot{\underset{\sim}{\varepsilon}}_g = \underset{\approx}{A}^C_g : \left(\dot{\underset{\sim}{E}} - \dot{\underset{\sim}{E}}^p\right) + \underset{\approx}{A}^C_g : \underset{\approx}{A}^B_g : \dot{\underset{\sim}{E}}^p + \underset{\approx}{A}^C_g : \underset{\approx}{S} : \left(\underset{\approx}{C}^{eff^{-1}} : \underset{\approx}{C}_g : \dot{\underset{\sim}{\varepsilon}}^p_g - \underset{\approx}{A}^B_g : \dot{\underset{\sim}{E}}^p\right) \tag{29}$$

The following transition rule is obtained:

$$\dot{\underset{\sim}{\sigma}}_g = \underset{\approx}{C}_g : \underset{\approx}{A}^C_g : \underset{\approx}{C}^{-1} : \dot{\underset{\sim}{\Sigma}} + \underset{\approx}{C}_g : \underset{\approx}{A}^C_g : \left(\underset{\approx}{S} - \underset{\approx}{I}\right) : \left(\dot{\underset{\sim}{\varepsilon}}^p_g - \underset{\approx}{A}^B_g : \dot{\underset{\sim}{E}}^p\right) \tag{30}$$

The effective viscoplastic strain rate is then deduced, applying self-consistency to Eq. (29):

$$\dot{\underset{\sim}{E}}^p = \left[\underset{\approx}{I} - \left\langle \underset{\approx}{A}^C_g : \left(\underset{\approx}{I} - \underset{\approx}{S}\right) : \underset{\approx}{A}^B_g \right\rangle\right]^{-1} : \left\langle \underset{\approx}{A}^C_g : \underset{\approx}{S} : \underset{\approx}{C}^{eff^{-1}} : \underset{\approx}{C}_g : \dot{\underset{\sim}{\varepsilon}}^p_g \right\rangle \tag{31}$$

During the computation stage, it is assumed that perturbations remain constant during a time increment. To avoid the implicit form of Eq. (28), perturbations are computed from the former increment (assuming that $\delta\underset{\approx}{c}_g(n=0) = \delta\underset{\approx}{b}_g(n=0) = \underset{\approx}{0}$). Thus:

$$\delta\underset{\approx}{c}_g(n) = \underset{\approx}{C}_g - \left\langle \underset{\approx}{C}_g : \left[\underset{\approx}{I} + \underset{\approx}{S}(n-1) : \underset{\approx}{C}^{eff^{-1}}(n-1) : \delta\underset{\approx}{c}_g(n-1)\right]^{-1} \right\rangle \tag{32}$$

$$\delta\underset{\approx}{b}_g(n) = \underset{\approx}{B}_g - \left\langle \underset{\approx}{B}_g : \left[\underset{\approx}{I} + \underset{\approx}{T}(n-1) : \underset{\approx}{B}^{eff^{-1}}(n-1) : \delta\underset{\approx}{b}_g(n-1)\right]^{-1} \right\rangle \tag{33}$$

3. Single crystal behavior

The mechanical behavior is represented by a crystal plasticity approach at the grain level. The model is first described, then the identification of the material parameters is made. The reference macroscopic mechanical behavior was taken from one-dimensional tensile tests performed on Inconel 718 specimens with equiaxed grains (Alexandre et al., 2004), The single crystal material parameters that best fit the experimental stress–strain curve of Inconel 718 are obtained following a two-step procedure:

- The cubic elasticity parameters $\left(\underset{\approx}{C}^0\right)$ are determined from the data of Hanriot et al. (1991) on AM1;
- The material parameters describing the viscoplastic behavior are then identified. For that purpose, a periodic FE aggregate is used to simulate a tensile test. The obtained stress–strain curve defining the average behavior of the polycrystal is scrutinized against the macroscopic experimental curve. Furthermore, it is demonstrated that the obtained material parameter set is successful for the full-field and the mean field approaches as well.

3.1. Elasticity

The degree of anisotropy of a cubic elasticity tensor $\underset{\approx}{C}$ can be described by a specific ratio, due to Zener:

$$\mathcal{Z} = \frac{2C_{2323}}{C_{1111} - C_{1122}} \tag{34}$$

It is assumed here that Inconel 718 has the same Zener ratio, Eq. (34), as AM1 ($\mathcal{Z} = 2.7$). Starting from the values of AM1 (Hanriot et al., 1991), the decomposition of the elasticity tensor provides the values of k', μ' and μ''

$$k' = \frac{C_{1111} + 2C_{1122}}{3}, \quad \mu' = \frac{C_{1111} - C_{1122}}{2} \quad \mu'' = C_{2323}$$

so that the shear modulus of a polycrystal of AM1 would be the solution of Eq. (35), as recalled in Appendix C.

$$f(\mu) = 8\mu^3 + (9k' + 4\mu')\mu^2 - (3k' + 12\mu')\mu''\mu - 6k'\mu'\mu'' = 0 \tag{35}$$

The value of the Young's modulus and Poisson's ratio are easily obtained, since the bulk modulus k and k' are the same:

$$E = \frac{9k\mu}{3k + \mu} \quad \text{and} \quad \nu = \frac{3k - 2\mu}{2(3k + \mu)} \tag{36}$$

The calibration of the cubic elasticity parameters follows then by scaling the AM1 parameters by means of the ratio (d) between the experimental Inconel 718 Young's modulus and the result of the previous computation on AM1 data. The results are given in Table 2.

Due to cubic symmetry, the apparent Young's modulus changes according to the tensile direction. The analytical function defining its variation is given in Appendix C. The Young's modulus reaches its maximum value for a stress along the $\langle 1\,1\,1 \rangle$ directions, a local extremum for the $\langle 1\,1\,0 \rangle$ directions, and the minimum value for the $\langle 1\,0\,0 \rangle$ directions.

The grains contained in a DS RVE are defined by changing only the angle θ of Fig. C.1. As a consequence,

- for a DS RVE loaded along the x_3 direction, the Young's modulus of all the grains will be $E_{\langle 100 \rangle}$,
- for a DS RVE loaded in the transverse direction, the Young's modulus will range from $E_{\langle 100 \rangle}$ to $E_{\langle 110 \rangle}$ (Fig. 4).

These local considerations can be helpful to select the representative orientations for the polycrystal: The resulting elastic tensor for DS material $\underset{\approx}{C}^{eff}$, computed by restricting Eq. (7) to elasticity, can be obtained from a 3 grain aggregate, (with $\theta = 0°, 60°, 120°$), or a 6 DS grain aggregate using the single crystal elasticity (see selected angles in Fig. 4). On the contrary, at least 300 grains are needed to get the correct HEM elasticity for a random polycrystal.

3.2. Viscoplasticity

3.2.1. Constitutive equations

Plastic flow is described by means of a crystal plasticity approach in small perturbations. According to the *fcc* structure of Nickel-base alloys, 12 slip systems of the octahedral family ($\{1\,1\,1\}$ planes and $\langle 1\,1\,0 \rangle$ directions) are introduced. The resolved shear stress τ^s, defining the stress state on a given slip system (s), is linked to the applied stress $\underset{\sim}{\sigma}_g$ of grain g through the Schmid tensor, $\underset{\sim}{m}^s$, which is built from the slip plane normal ($\underline{n}^s$) and the slip direction ($\underline{l}^s$):

$$\tau^s = \underset{\sim}{\sigma}_g : \underset{\sim}{m}^s \quad \text{with } \underset{\sim}{m}^s = \frac{1}{2}(\underline{l}^s \otimes \underline{n}^s + \underline{n}^s \otimes \underline{l}^s) \tag{37}$$

Each slip system has its own criterion:

$$f^s(\tau^s, x^s, r^s) = |\tau^s - x^s| - r^s \tag{38}$$

where x^s and r^s are respectively the kinematic and isotropic hardening variables, with the following non-linear evolution rules:

$$x^s = c\alpha^s \quad \text{with } \dot{\alpha}^s = (\eta^s - d\alpha^s)\dot{v}^s \tag{39}$$

$$r^s = \tau_c^s + Q\sum_r h_{sr} b\rho^r \quad \text{with } \dot{\rho}^r = (1 - b\rho^r)\dot{v}^r \tag{40}$$

where $\dot{v}^s$ is the cumulated shear strain rate, τ_c^s is the critical resolved shear stress (CRSS) beyond which the slip system is activated. The h_{sr} terms belong to the matrix which defines the interaction between the different slip systems and η^s is the sign of $(\tau^s - x^s)$.

The cumulated shear strain rate is defined through a power law:

$$\dot{v}^s = \left\langle \frac{f^s}{K} \right\rangle^n \tag{41}$$

The viscoplastic strain rate in each grain results from the contribution of all the active slip systems:

$$\underset{\sim}{\dot{\varepsilon}}_g^p = \sum_s \dot{v}^s \eta^s \underset{\sim}{m}^s \tag{42}$$

Note that, for the "Translated Field" model, the expression of the instantaneous local secant viscoplastic moduli, $\underset{\approx}{B}_g$, is required, Eq. (43). Due to incompressibility, the fourth order tensor that comes from the theory cannot be inverted. Following (Paquin et al., 2001), a negligible compressible contribution ($\underset{\approx}{\Lambda}^c$) will then be added to compute the inverse according to:

$$\underset{\approx}{B}_g = \left[\sum_s \frac{n}{K} \left\langle \frac{|\tau^s - x^s| - r^s}{K} \right\rangle^{n-1} \underset{\sim}{m}^s \otimes \underset{\sim}{m}^s + \underset{\approx}{\Lambda}^c \right]^{-1} \tag{43}$$

3.2.2. Parameter identification

Onedimensional tensile tests are simulated on a 100 Voronoï grain aggregates with periodic boundaries (Fig. 5), and random crystal orientations. The mechanical behavior of each grain is predicted by the cubic elasticity constants given in Table 2 and the constitutive equations defined in Section 3.2.1. Since the hardening modulus is very low (Fig. 6) the material parameters Q and c are equal to 0.

The identification process concerns then only the two parameters defining the (low) viscous effect (n and K) and the CRSS, τ_c. They are obtained by comparison between the overall response of the aggregate and the reference σ–ε curve from (Alexandre

Table 2
Elasticity constants of the cubic single crystal in GPa, Young's modulus (GPa) and Poisson's ratio of the homogenized polycrystal, in the case of AM1 and Inconel 718 ($d = 0.877$).

Alloy	Single crystal			Polycrystal	
	C_{1111}	C_{1122}	C_{2323}	E	ν
AM1 (Hanriot et al., 1991)	296	204	125	227	0.338
Inconel 718	259.6	179	109.6	199	0.338

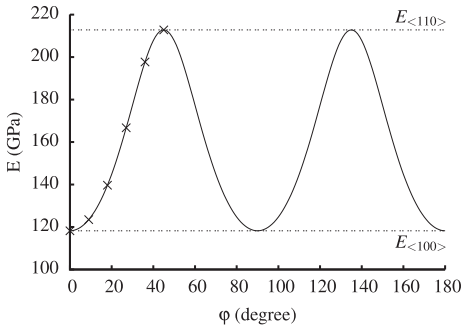

Fig. 4. Young's modulus evolution of a DS single crystal of Inconel 718, with respect to the orientation φ of the applied uniaxial stress. Crosses indicate the specific angles chosen for the computation of the HEM elasticity tensor.

et al., 2004) experimental work. The fitted values are given in Table 3.

The consistency of these parameters is demonstrated through a series of numerical simulations, performed on:

- A full-field model of 100 grains (Fig. 6), where the effect of elastic anisotropy is highlighted.
- Two mean-field models with 400 grains (Fig. 7), with either isotropic (Berveiller–Zaoui) or cubic ("Translated Field") elasticity, which have been implemented in ZSet/Zébulon FE code (Transvalor and ENSMP, 2010).

3.3. Application to various microstructure

Fig. 8 shows the behavior of a single crystal and of a DS material element. The tensile load direction is perpendicular to the x_3 axis. As expected, the smallest apparent Young's modulus is obtained for $\langle 1\,0\,0\rangle$ direction ($\theta = 0°$) and the largest for $\langle 1\,1\,0\rangle$ ($\theta = 45°$). Both curves end at the same stress value, since the corresponding Schmid factors are the same. A rotation of 60° provides an intermediate Young's modulus and a weak viscoplastic response. The DS response is built by means of a mixture of these various grains, and presents intermediate values for both Young's modulus and ultimate stress. Fig. 9 proposes a comparison between the DS RVE loading in three different directions (axial, transverse and 30° with respect to the x_3 axis) and two isotropic aggregates. Fortunately, it can be checked that the response of the aggregate does not depend on the tensile direction, that demonstrates its representative character. Due to the presence of $\langle 1\,1\,1\rangle$ orientations, these aggregates have a larger apparent Young's modulus if compared with axial and transverse responses of the DS material. Again, the axial direction has the smallest Young's modulus, but its ultimate stress is larger than the transverse, since the latter offers larger Schmid factor. In fact, a DS RVE loaded in x_3 axis does not develop any internal stress, since, due to the specific form of Eshelby's tensor, the axial strain is uniform in the aggregate ($\varepsilon_{g33} = E_{33}$): it behaves like a single crystal. Finally, it can be pointed out that the strongest response is obtained for a DS material loaded with a tensile axis at 30° with respect to x_3.

4. FE analysis of notched component

In this section, FE computations are performed, using the full-field and the mean-field models described and identified in the previous sections, to evaluate their ability to predict the mechanical behavior and the resulting stress distribution of a notched component subjected to an uniaxial loading path. A 3D mesh (Fig. 10) with 13 696 quadratic elements and 243 960 nodes is used for the FE analysis of the structure. The pressure imposed on the top surface along the x_2 direction increases linearly during the time step and reaches 75 MPa after 12 s.

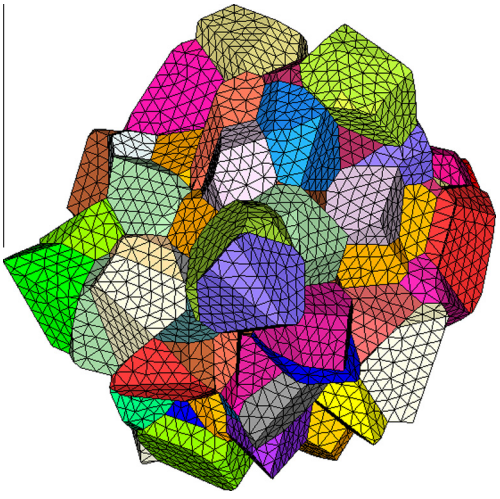

Fig. 5. Periodic FE 100 Voronoï grain aggregate.

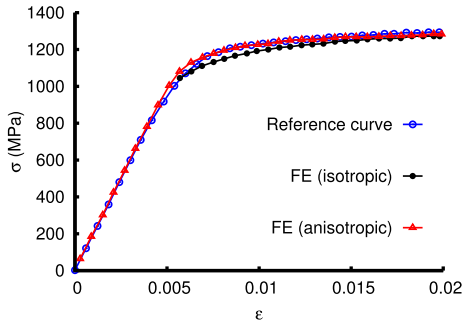

Fig. 6. Stress–strain curves obtained for a onedimensional tensile loading on a FE periodic aggregate composed of 100 grains. The reference experimental tensile test was performed on Inconel 718 by Alexandre et al. (2004).

Table 3
Viscoplastic set of parameters for Inconel 718.

K (MPa$^{1/n}$)	n	τ_c (MPa)
13	20	465

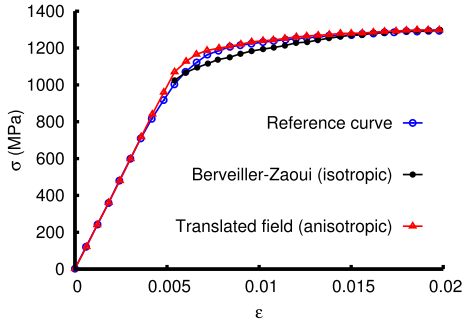

Fig. 7. Stress–strain curves obtained for a onedimensional tensile loading on a mean-field model composed of 400 grains. The reference experimental tensile test was performed on Inconel 718 by Alexandre et al. (2004).

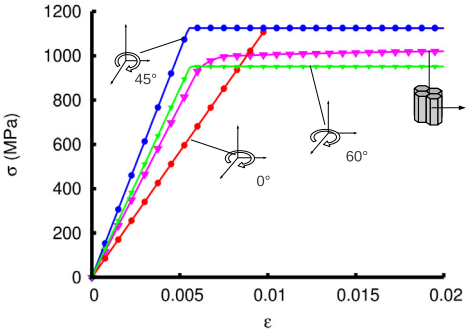

Fig. 8. Stress–strain curves simulated with the translated field model for a transversely tensile loading considering a 400 DS grain aggregate and various single crystal orientations.

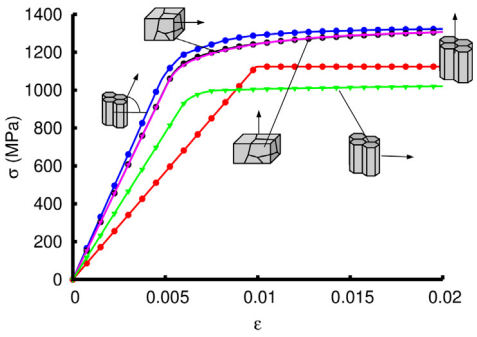

Fig. 9. Stress–strain curves simulated with the translated field model for equiaxed and DS aggregates (400 grains) under various tensile directions.

This component is made of small Inconel 718 equiaxed grains, whereas the grains across the section in the notch for which the behavior can be explicitly represented by DS grains, Fig. 10(b), or by a mean-field model, Fig. 10(c). However, it seems unnecessary to represent the behavior of the jaw at a microscopic level. As a matter of fact, the stress will be mainly localized in the notch part. The macroscopic model given by Alexandre et al. (2004) will therefore be used to describe this equiaxed microstructure. Finally, three distinct representations of the structure will be investigated:

- As a reference, a simulation will be performed using the macroscopic behavior for the entire component, Fig. 10(a);
- The DS microstructure in the notch can be explicitly represented by defining 56 bulk DS grains. For each grain, constitutive equations are defined through the parameters set fitted in the previous section (Table 3). A random crystal orientation is attributed. Isotropic and anisotropic elasticity of the single crystal will be investigated. Moreover, to obtain a large number of possible configurations, 20 simulations corresponding to different sets of grain orientations are performed;
- A single simulation is performed using translated field (Section 2.3) and uniform elasticity Kröner's rule (Section 2.2.2) models, respectively. For that purpose, the 6 grain aggregate defined earlier (selected rotations shown in Fig. 4) is attributed to each Gauss point of the notched part.

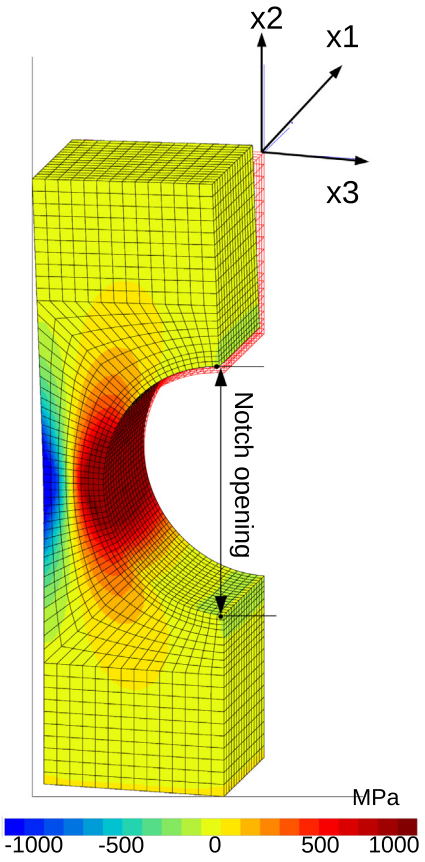

Fig. 11. Stress along x_2 obtained for a 75 MPa loading with uniform elasticity Kröner mean field model.

In Fig. 11, obtained with the uniform elasticity Kröner model for a 75 MPa loading, one can notice that the notch is in tension, while the opposite part is in compression. This is caused by the notch opening, for which the upper jaw is moving with the applied pressure, and the lower jaw remains fixed. A first comparison between models can be made from the evolution of this notch opening (Fig. 12).

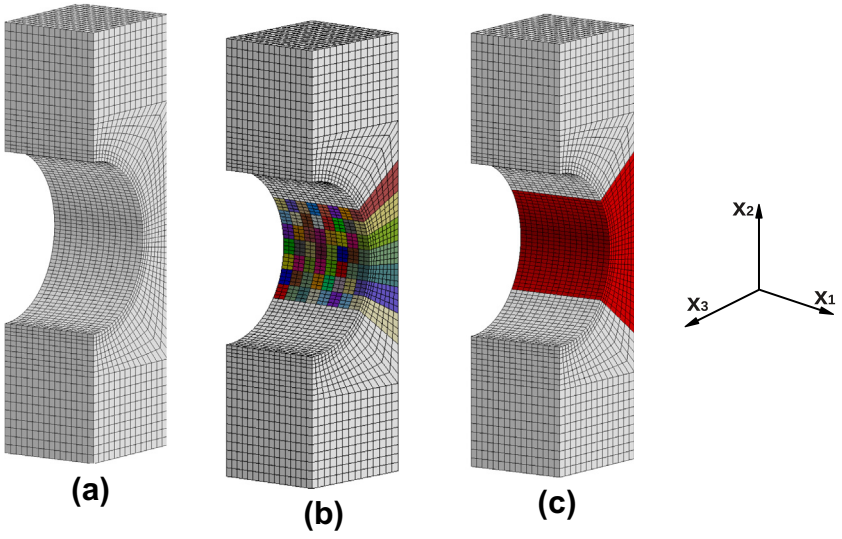

Fig. 10. The three different approaches for the representation of the FE notched component. (a) Macroscopic, (b) full-field with 20 random sets, (c) mean field with one selected set.

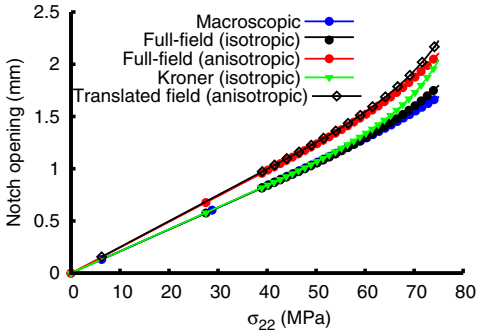

Fig. 12. Notch opening evolution with the applied stress, for the different models involved.

Fig. 12 shows that a softer strain response is obtained when anisotropic elasticity is considered, which leads to a larger reversible notch opening. This is linked to the fact that the applied load is transverse to the solidification direction of the grains, so that the directions that have high elastic moduli (like $E_{\langle 111\rangle}$ in Eq. (C.4)) are not present in the DS microstructure. This effect is captured by the two approaches that introduce anisotropy (full field FE calculation and translated field model). On the contrary, the isotropic elasticity results from the equiaxed structure, with all the possible directions, and predicts a higher elastic modulus.

The stiffest mechanical response in the plastic regime is given by the macroscopic model. This approach is then far too optimistic as long as the displacements of the structure are concerned. This result is even true for the full field FE model, where uniform elasticity prevents the material to develop plasticity. Full field anisotropic behavior is much softer. The elastic slope obtained with the translated field model is in agreement with full field anisotropy: it demonstrates that the number of orientations is sufficient for the elastic regime. The opening is then a little larger for the plastic regime, but the difference remains reasonable. Interestingly, Kröner's model, that is harder than translated field approach in the elastic regime, exhibits the largest plastic flow. This can be explained by the high level of internal stresses that is locally accumulated.

Having in hand the macroscopic response is not enough to prepare a good estimation of the lifetime. The next three figures are then devoted to an analysis of the local responses. Fig. 13 shows the axial stress–strain curves on the grain level, and the other two figures (Figs. 14 and 15) illustrate the stress distribution.

Fig. 13 illustrates the effect of heterogeneous elasticity, by plotting the stress–strain curves along x_2 axis for each node which belongs to the inner surface of the notch, at the center of each grain. For the two cases which introduce uniform isotropic elasticity, namely the isotropic full field calculation (top left) and Kröner's model (bottom left), there is obviously no scatter during the elastic regime. In fact, significant internal stresses are present in the more realistic computations, anisotropic full field (top right) and translated fields (bottom right). As a consequence, the scatter during the elastoplastic regime is also underestimated by the models with isotropic uniform elasticity. The effect can be quantified by considering the stress distribution for 1% strain in each calculation, as mentioned in the four graphs. For the case of Kröner's model (bottom left), the range between the minimum and the maximum stress is less than 100 MPa. Local strain incompatibilities due to plastic flow increase the internal stresses, so that the preceding range reaches 250 MPa for the full field isotropic calculation. The translated field model (bottom right) has a smaller scatter range. That might be due to the relatively low number of grains, and also to the averaging character of the model. Nevertheless, this model has a good representation of the heterogeneity in the elastic regime, and it remains in reasonable agreement with the full field anisotropic calculation for the plastic regime. As a general remark, it must be noted that some elastically soft grains may present very large strains, meanwhile strong grains do not even reach 1% strain.

The stress level for a 1% strain is used to present an histogram of the stress distribution (Fig. 14). For the full field approach, the curve results from an average of the 20 simulations, as illustrated by Fig. 15. For all the distributions, the macroscopic reference reached in the notch (1200–1250 MPa) represents an upper bound. The class of stress larger than 1150 MPa is very small for all the

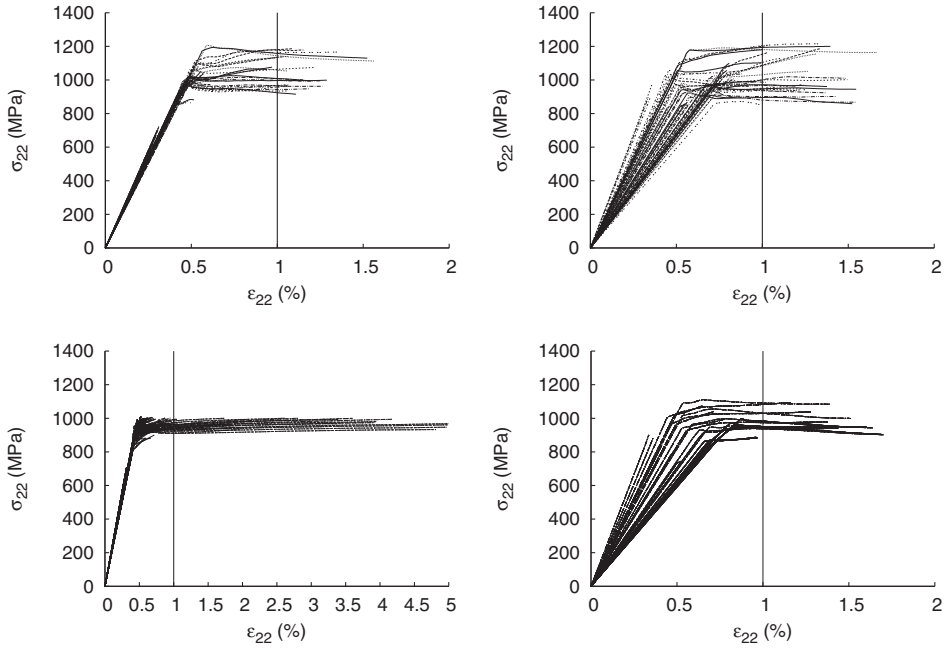

Fig. 13. Stress–strain curves in the x_2 direction for each DS grain in the full-field isotropic (top left) and anisotropic (top right) models, and in the mean-field uniform elasticity Kröner (bottom left) and "translated field" (bottom right) models.

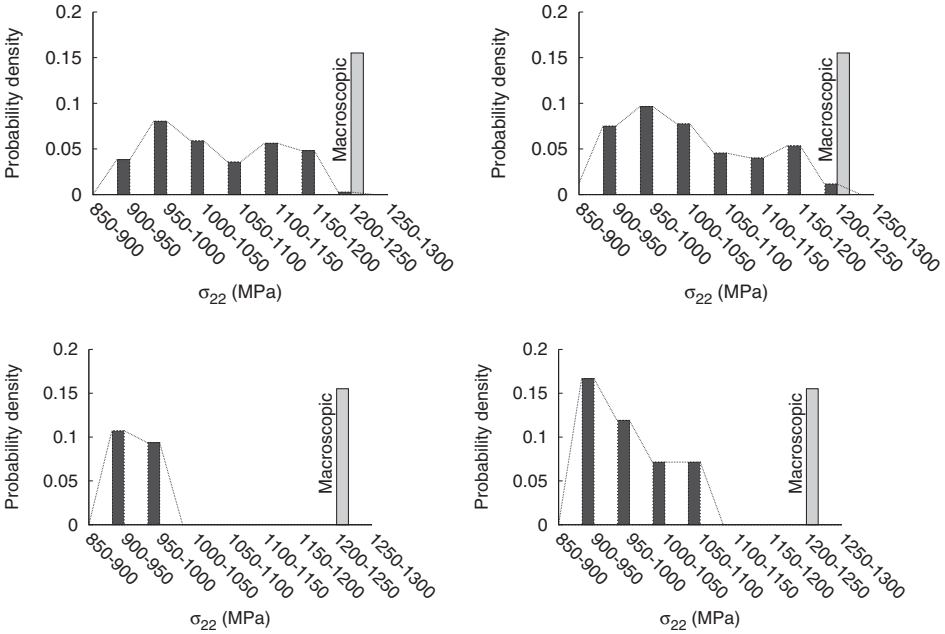

Fig. 14. Stress distributions for the full-field computations (average on the 20 sets of random grains) in the isotropic (top left) and the anisotropic cases (top right). Comparison with uniform elasticity Kröner's model computation (bottom left) and "translated field" (bottom right). The reference for all the histograms is the macroscopic stress.

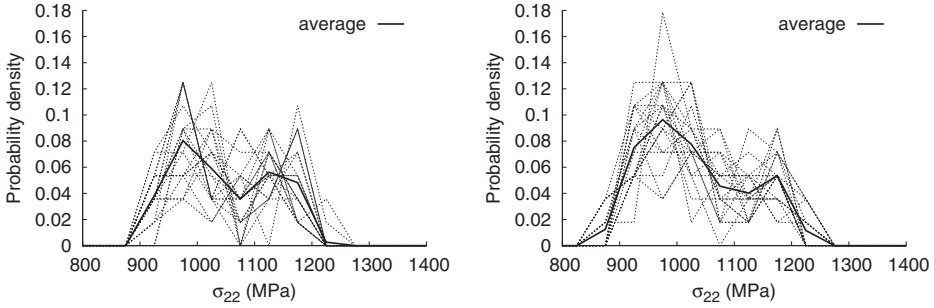

Fig. 15. Average of the 20 simulated stress distributions obtained with various sets of crystal orientations, in the isotropic (left) and anisotropic (right) cases.

curves. The comparison between the two full field computations (isotropic and anisotropic local elasticity) confirms that the stress distributions are almost similar (Fig. 14). This means that the model built with the "isotropic" assumption is able to correctly describe stress distributions in the elastoplastic regime, even if it is very far from the anisotropic case in elasticity. The stress distributions attached to the two mean field models are too narrow. Kröner's model is specially too optimistic, since it underestimates the maximum local stress in the critical grains, and must be avoided. The translated field model remains a good candidate for a fast estimation of the local scatter.

Fig. 15 gives a more detailed view on the local fields. It is worth noting that, depending on the realization, the probability density for a given class may present large variations. This point does not alter the previous conclusions, since the stress range remains constant for all the cases.

5. Conclusion

The main purpose of the model was to investigate several solutions to deal with large grain microstructures in industrial parts, with a special attention to columnar grains that are present in thin walls. Strictly speaking, each new component corresponds to a new set of crystallographic orientations, so that it should be considered as an other structure. This is why, taking the example of a notched specimen with large columnar grains at the notch root, we started performing a set of full field computations, allowing us to build a reference data base that characterizes the scatter resulting from the various orientations. Twenty calculations were performed to achieve this section of the study. It has then be demonstrated that an alternative strategy can provide the same result by means of a single calculation. This has been made by using a uniform field model on each integration point in the structural computation. Since it introduces local stress redistribution, this model can reproduce the occurrence of the various orientations, so that it delivers a satisfactory estimation of the scatter obtained with the full field model.

In order to be successful, this alternative computation route must introduce a realistic uniform field model. A specific attention was paid to the contribution of elastic heterogeneities. Two kinds of mean-field models have been introduced. The first one, based on translated field self-consistent scheme, aims at describing both local elastic and plastic anisotropy. The second one, namely a Kröner type transition rule with uniform elasticity, focuses only on plastic heterogeneities. These models have been extended to equiaxed and DS microstructures. Due to the intergranular accommodation, the hardening is more pronounced for the model

involving a local anisotropic elasticity, that cumulates elastic and plastic anisotropy effects. Only this model was in good agreement with FE computations.

The calibration procedure used experimental data taken from a polycrystalline Inconel 718. A full field model of a representative material element has been built to determine the material parameters of the grain. The model assumes that there is no preferential crystallographic orientation, and that each grain in the aggregate can be modeled by crystal plasticity constitutive equations. Uniaxial tensile test simulations were performed on the aggregate and compared with the macroscopic stress–strain response. This crystal plasticity model was then be introduced in the component model. An other assumption is then that the material parameters obtained with the small equiaxed grains of the RVE can be used for the large grains in the component.

This new computational methodology has been compared with a pure macroscopic calculation. It is shown that the computation made with the macroscopic model overestimates the critical stress at the notch root. The framework proposed here allows to take into account any microstructure gradient in a component, since one can imagine to continuously shift from a uniform field crystal plasticity model in the critical areas to a simple von Mises model in the places with a regular grain size. In the present state, the proposed approach is very efficient in terms of computer CPU time, since it introduces 6 grains only to generate the local scatter. The next step of the study is to introduce an experimental verification of these estimations. Specifically, local strain field measurements should be made on large grain specimens and compared with the numerical prediction. The assumption that the constitutive equations obtained on the equiaxed grain can be used for the large grains is also questionable, but, if needed, a size effect can also be introduced in the model.

Appendix A. Elasticity and Eshelby's tensors for particular symmetries

In Section 2.2.1, it was mentioned that an isotropic tensor could be decomposed by using the operators $\underset{\approx}{K}$ and $\underset{\approx}{J}$. For a cubic symmetry, such a decomposition can also be achieved by splitting $\underset{\approx}{J}$ into two parts: $\underset{\approx}{J} = \underset{\approx}{J'} + \underset{\approx}{J''}$. In these conditions, the cubic elasticity tensor writes:

$$\underset{\approx}{C} = 3k' \underset{\approx}{K} + 2\mu' \underset{\approx}{J'} + 2\mu'' \underset{\approx}{J''} \tag{A.1}$$

with

$$K_{ijkl} = \frac{1}{3}\delta_{ij}\delta_{kl}$$

$$J'_{ijkl} = \delta_{pi}\delta_{pj}\delta_{pk}\delta_{pl} - \frac{1}{3}\delta_{ij}\delta_{kl}$$

$$J''_{ijkl} = \frac{1}{2}\left(\delta_{ik}\delta_{jl} + \delta_{il}\delta_{jk}\right) - \delta_{pi}\delta_{pj}\delta_{pk}\delta_{pl}$$

where δ_{ij} is the Kronecker delta.

The three constants k', μ' and μ'' are given by:

$$k' = \frac{C_{1111} + 2C_{1122}}{3}, \quad \mu' = \frac{C_{1111} - C_{1122}}{2}, \quad \mu'' = C_{2323}$$

In the following, the effective isotropic elasticity, represented here by k and μ, is related to the local cubic elasticity, represented by k', μ' and μ''. The homogenization equation applied to elasticity Eq. (7) is rewritten as:

$$\left\langle \left(\underset{\approx}{C_g} - \underset{\approx}{\Lambda}\right) : \left[\underset{\approx}{I} - \underset{\approx}{S} : \left(\underset{\approx}{I} - \underset{\approx}{\Lambda}^{-1} : \underset{\approx}{C_g}\right)\right]^{-1} \right\rangle = \underset{\approx}{0} \tag{A.2}$$

and then expressed according to $\underset{\approx}{K}$, $\underset{\approx}{J'}$ and $\underset{\approx}{J''}$:

$$\frac{3(k-k')}{1-\alpha\left(1-\frac{k'}{k}\right)}\left\langle \underset{\approx}{K} \right\rangle + \frac{2(\mu-\mu')}{1-\beta\left(1-\frac{\mu'}{\mu}\right)}\left\langle \underset{\approx}{J'} \right\rangle + \frac{2(\mu-\mu'')}{1-\beta\left(1-\frac{\mu''}{\mu}\right)}\left\langle \underset{\approx}{J''} \right\rangle = \underset{\approx}{0} \tag{A.3}$$

All the constants used in the previous equation are the same for all the grains of the polycrystal. Thus, they are stepped out of the homogenization operation. Moreover, it is well established that:

$$\left\langle \underset{\approx}{K} \right\rangle = \underset{\approx}{K}, \quad \left\langle \underset{\approx}{J'} \right\rangle = \frac{2}{5}\underset{\approx}{J}, \quad \left\langle \underset{\approx}{J''} \right\rangle = \frac{3}{5}\underset{\approx}{J} \tag{A.4}$$

Introducing two constants a and b, Eq. (A.3) leads to:

$$a\underset{\approx}{K} + b\underset{\approx}{J} = \underset{\approx}{0} \tag{A.5}$$

The two following conditions are mandatory:

- $a = 0$, which implies that $k = k'$;
- $b = 0$, which leads to a third degree equation:

$$f(\mu) = 8\mu^3 + (9k' + 4\mu')\mu^2 - (3k' + 12\mu')\mu''\mu - 6k'\mu'\mu'' = 0 \tag{A.6}$$

Knowing the values of k', μ' and μ'', the value of the elastic parameters for the isotropic polycrystal can be easily deduced.

Appendix B. Eshelby's problem of an inclusion embedded in an infinite medium

The single crystal elasticity tensor has a cubic symmetry:

$$\underset{\approx}{C^0} = \begin{pmatrix} C^0_{1111} & C^0_{1122} & C^0_{1122} & 0 & 0 & 0 \\ C^0_{1122} & C^0_{1111} & C^0_{1122} & 0 & 0 & 0 \\ C^0_{1122} & C^0_{1122} & C^0_{1111} & 0 & 0 & 0 \\ 0 & 0 & 0 & C^0_{2323} & 0 & 0 \\ 0 & 0 & 0 & 0 & C^0_{2323} & 0 \\ 0 & 0 & 0 & 0 & 0 & C^0_{2323} \end{pmatrix} \tag{B.1}$$

while, the HEM elasticity tensor for a DS microstructure has a transversely isotropic symmetry:

$$\underset{\approx}{C} = \begin{pmatrix} C_{1111} & C_{1122} & C_{1133} & 0 & 0 & 0 \\ C_{1122} & C_{1111} & C_{1133} & 0 & 0 & 0 \\ C_{1133} & C_{1133} & C_{3333} & 0 & 0 & 0 \\ 0 & 0 & 0 & C_{2323} & 0 & 0 \\ 0 & 0 & 0 & 0 & C_{2323} & 0 \\ 0 & 0 & 0 & 0 & 0 & \frac{C_{1111}-C_{1122}}{2} \end{pmatrix} \tag{B.2}$$

According to Suvorov and Dvorak (2002), the Eshelby's non-zero constants for an infinite cylindrical ($a_1 = a_2 \ll a_3$) inclusion are:

Transversely isotropic

HEM

$$S_{1111} = \frac{5C_{1111} + C_{1122}}{4C_{1111}}$$

$$S_{1122} = \frac{3C_{1122} - C_{1111}}{4C_{1111}}$$

$$S_{1133} = \frac{C_{1133}}{2C_{1111}}$$

$$S_{1212} = \frac{3C_{1111} - C_{1122}}{4C_{1111}}$$

$$S_{2323} = \frac{1}{4} \tag{B.3}$$

Full isotropic

HEM

$$S_{1111} = \frac{5-4\nu}{8(1-\nu)}$$
$$S_{1122} = \frac{4\nu-1}{8(1-\nu)}$$
$$S_{1133} = \frac{\nu}{2(1-\nu)}$$
$$S_{1212} = \frac{3-4\nu}{8(1-\nu)}$$
$$S_{2323} = \frac{1}{4} \tag{B.4}$$

While the Eshelby's tensor, according to Mura (1987), for spherical inclusions in a isotropic HEM is:

$$\underset{\approx}{S} = \begin{pmatrix} S_{1111} & S_{1122} & S_{1122} & 0 & 0 & 0 \\ S_{1122} & S_{1111} & S_{1122} & 0 & 0 & 0 \\ S_{1122} & S_{1122} & S_{1111} & 0 & 0 & 0 \\ 0 & 0 & 0 & S_{2323} & 0 & 0 \\ 0 & 0 & 0 & 0 & S_{2323} & 0 \\ 0 & 0 & 0 & 0 & 0 & S_{2323} \end{pmatrix}$$

$$S_{1111} = \frac{7-5\nu}{15(1-\nu)}$$
$$S_{1122} = \frac{5\nu-1}{15(1-\nu)} \tag{B.5}$$
$$S_{2233} = \frac{4-5\nu}{15(1-\nu)}$$

Appendix C. Homogenisation of a random cubic polycrystal in elasticity

The apparent Young's modulus of a cubic single crystal can be defined analytically. Considering a random unilateral stress, its orientation is defined thanks to two angles (φ, θ):

The stress and strain along the normal $\underline{n}$ are:

$$\sigma = \underset{\sim}{\sigma} : (\underline{n} \otimes \underline{n})$$
$$\varepsilon = \underset{\sim}{\varepsilon} : (\underline{n} \otimes \underline{n})$$
$$\text{with} : \underset{\sim}{\sigma} = \underset{\approx}{C} : \underset{\sim}{\varepsilon}$$

In the case of a one-dimensional tensile test along $\underline{n}$, it can also be written:

$$\underset{\sim}{\sigma} = \sigma(\underline{n} \otimes \underline{n})$$
$$\text{with} : \sigma = E\varepsilon$$

It can be deduced from the previous relations that:

$$\frac{1}{E} = \underset{\approx}{\mathcal{N}} : \underset{\approx}{C^{-1}} : \underset{\sim}{\mathcal{N}} \tag{C.1}$$

with:

$$\underset{\approx}{\mathcal{N}} = \underline{n} \otimes \underline{n} = \begin{pmatrix} \sin^2(\varphi)\cos^2(\theta) & \sin^2(\varphi)\cos(\theta)\sin(\theta) & \sin(\varphi)\cos(\varphi)\cos(\theta) \\ & \sin^2(\varphi)\sin^2(\theta) & \sin(\varphi)\cos(\varphi)\sin(\theta) \\ \text{sym} & & \cos^2(\varphi) \end{pmatrix}$$

By decomposition of the cubic elasticity tensor Eq. (A.1), introducing $\underset{\approx}{K}$, $\underset{\approx}{J'}$ and $\underset{\approx}{J''}$, the following equation is obtained:

$$\frac{1}{E} = \left(\frac{1}{9k'} - \frac{1}{6\mu'}\right) + \left(\frac{1}{2\mu'} - \frac{1}{2\mu''}\right)\left(\mathcal{N}_{11}^2 + \mathcal{N}_{22}^2 + \mathcal{N}_{33}^2\right) + \frac{1}{2\mu''}\left[\left(\mathcal{N}_{11}^2 + \mathcal{N}_{22}^2 + \mathcal{N}_{33}^2\right) + 2\left(\mathcal{N}_{23}^2 + \mathcal{N}_{31}^2 + \mathcal{N}_{12}^2\right)\right]$$

Expressing the terms of $\underset{\approx}{\mathcal{N}}$ in trigonometric form, the previous equation can be simplified. In particular, it can be noticed that:

$$\left[\left(\mathcal{N}_{11}^2 + \mathcal{N}_{22}^2 + \mathcal{N}_{33}^2\right) + 2\left(\mathcal{N}_{23}^2 + \mathcal{N}_{31}^2 + \mathcal{N}_{12}^2\right)\right] = 1$$

Thus

$$\frac{1}{E} = \left(\frac{1}{9k'} - \frac{1}{6\mu'}\right) + \left(\frac{1}{2\mu'} - \frac{1}{2\mu''}\right) f(\varphi, \theta) + \frac{1}{2\mu''} \tag{C.2}$$

with $f(\varphi, \theta) = sin^4(\varphi) + cos^4(\varphi) - 2sin^4(\varphi)sin^2(\theta)cos^2(\theta)$

It is worth noting that, in the isotropic case ($\mu = \mu' = \mu''$), the second term of the equation is zero. The Young's modulus is therefore independent of the stress direction Eq. (36). Using Eq. (C.2), the evolution of the apparent Young's modulus of a single crystal as function of the loading direction can be plotted as shown in Fig. C.2. Three different extremums can be observed on that figure. They correspond to the stress directions along $\langle 100 \rangle, \langle 110 \rangle$ and $\langle 111 \rangle$. To evaluate their expressions, the function $f(\varphi, \theta)$ is derived:

$$\begin{cases} \frac{\partial f(\varphi,\theta)}{\partial \theta} = 0 \Rightarrow \sin^4(\varphi)\sin(\theta)\cos(\theta)\cos(2\theta) = 0 \\ \frac{\partial f(\varphi,\theta)}{\partial \varphi} = 0 \Rightarrow \cos(\varphi)\sin(\varphi)\left(\cos(2\varphi) + 2\sin^2(\varphi)\sin^2(\theta)\cos^2(\theta)\right) = 0 \end{cases} \tag{C.3}$$

As expected, $\{\varphi, \theta\}$ obtained after solving the system (C.3) defines the particular direction families mentioned above. Young's modulus extremums can then be expressed:

$$\begin{cases} f(\varphi,\theta) = \frac{1}{3} & \Rightarrow & E_{\langle 111 \rangle} = \frac{9k'\mu''}{3k'+\mu''} \\ f(\varphi,\theta) = \frac{1}{2} & \Rightarrow & E_{\langle 110 \rangle} = \frac{36k'\mu'\mu''}{4\mu'\mu''+3k'\mu''+9k'\mu'} \\ f(\varphi,\theta) = 1 & \Rightarrow & E_{\langle 100 \rangle} = \frac{9k\mu'}{3k'+\mu'} \end{cases} \quad \text{with } E_{\langle 111 \rangle} \rangle E_{\langle 110 \rangle} \rangle E_{\langle 100 \rangle}. \tag{C.4}$$

Appendix D. Evolution of Young's modulus with the loading direction in a cubic single crystal

Consider an infinite homogeneous medium (Ω) subjected to an uniform strain, and perturbed by an inclusion (or a cavity). If a stress free strain ε_{kl}^L is applied within the inclusion, the Hooke's law gives:

$$\sigma_{ij} = C_{ijkl}(\varepsilon_{kl} - \varepsilon_{kl}^L) = C_{ijkl}(u_{l,k} - \varepsilon_{kl}^L) \tag{D.1}$$

where $\underset{\approx}{C}$ is the medium elasticity tensor. Equations of equilibrium for a material domain free from any external force and any surface constraint are:

$$\sigma_{ij,j} = C_{ijkl}\varepsilon_{kl,j} - C_{ijkl}\varepsilon_{kl,j}^L = 0 \quad (i = 1, 2, 3) \tag{D.2}$$

The contribution of the eigenstrain ε^L to the equations of equilibrium is similar to that of a body force. One can thus make the

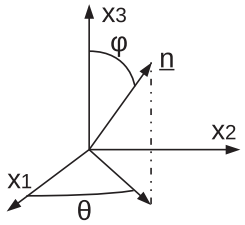

$$\underset{\sim}{n} = \begin{pmatrix} sin(\varphi)cos(\theta) \\ sin(\varphi)sin(\theta) \\ cos(\varphi) \end{pmatrix}$$

Fig. C.1. Angles defining a tensile direction n in the laboratory frame

comparison with the problem of finding the displacement at a point x when a force F is applied on an other point x'. The medium being homogeneous and infinite, the solution will simply depend on the distance between these two points $(x - x')$:

$$u_i(x) = u_i^0(x) + \int_\Omega G_{ij}(x - x')F_j(x')d\Omega' \tag{D.3}$$

$$u_i(x) = u_i^0(x) - \int_\Omega G_{ij}(x - x')C_{jpkl}\varepsilon^L_{kl,p'}d\Omega' \tag{D.4}$$

where $\underset{\sim}{G}$ is the Green tensor and $u_i^0(x)$ is the displacement from the reference medium to boundaries conditions. In our case, the medium is characterized by an uniform elasticity tensor $\underset{\approx}{C}$, thus $u_i^0(x)$ is zero. Eq. (D.4) can be further developed, which leads to:

$$u_i(x) = -\int_\Omega C_{jpkl}G_{ij}(x - x')\varepsilon^L_{kl}n_{p'}d\Omega' + \int_\Omega C_{jpkl}G_{ij,p'}(x - x')\varepsilon^L_{kl}d\Omega' \tag{D.5}$$

where n_p is the exterior unit normal vector on the boundary of the domain Ω. First term of Eq. (D.5) has to be zero because surfaces are traction free. For a uniform eigenstrain and in the case where the point x is inside the ellipsoid (Fig. D.1), the previous Eq. (D.3) can be developed according to Mura (1987):

$$u_i(x) = \frac{1}{4\pi}C_{jlmn}\varepsilon^L_{nm}x_k\int_{-1}^{1}\int_0^{2\pi}\frac{\xi_k\xi_l N_{ij}(\underline{\xi})}{D(\underline{\xi})}d\theta d\zeta_3 \tag{D.6}$$

where $\underline{\xi}$ is the wave vector introduced by the Fourier transform (see Mura, 1987). The volume integration of the infinite medium has been reduced to the contour integral of a unit sphere, which is defined by the unit vector $\underline{\zeta}$. As shown in Fig. D.1, any point within the unit sphere can be described by the pair (ζ_3, θ). The relations between the $\underline{\xi}$-space and the $\underline{\zeta}$-space are:

$$\xi_1 = \frac{\sqrt{1-\zeta_3^2}}{a_1}\cos\theta, \quad \xi_2 = \frac{\sqrt{1-\zeta_3^2}}{a_2}\sin\theta, \quad \xi_3 = \frac{\zeta_3}{a_3} \tag{D.7}$$

In Eq. (D.6), the constants N_{ij} and D are respectively the cofactors and the determinant of the second-rank tensor $\underset{\sim}{K}$:

$$K_{ik}(\underline{\xi}) = C_{ijkl}\xi_j\xi_l \tag{D.8}$$

$$D(\underline{\xi}) = \epsilon_{mnl}K_{m1}K_{n2}K_{l3} \tag{D.9}$$

$$N_{ij}(\underline{\xi}) = \frac{\epsilon_{ikl}\epsilon_{jmn}}{2}K_{km}K_{ln} \tag{D.10}$$

where ϵ_{ijk} is the Levi–Civita symbol.

Eshelby (1957) has proposed to relate the total strain to the stress free strain with the so called Eshelby tensor:

$$\underset{\sim}{\varepsilon} = \underset{\approx}{S} : \underset{\sim}{\varepsilon^L} \tag{D.11}$$

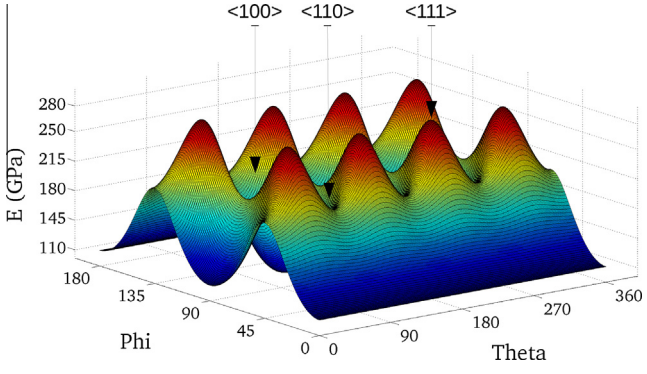

Fig. C.2. Young's modulus evolution of a cubic single crystal as a function of the two angles defining the loading direction, for the elasticity constants of Inconel 718 defined in Table 2.

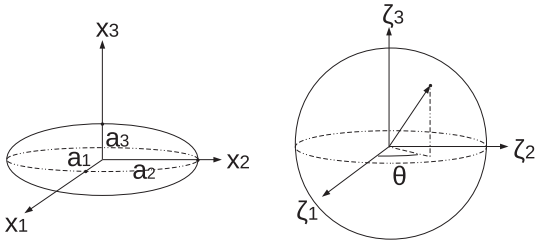

Fig. D.1. (left), an ellipsoidal inclusion with principal half axes a_1, a_2 and a_3. (right), the unit sphere which is equivalent to the infinite uniform medium.

From the expression of the displacement in function of the eigenstrain (D.6), one can deduce the expression of the Eshelby tensor:

$$S_{ijmn} = \frac{1}{8\pi}C_{pqmn}\int_{-1}^{1}\int_0^{2\pi}\left(\frac{\xi_j\xi_q N_{ip}(\underline{\xi}) + \xi_i\xi_q N_{jp}(\underline{\xi})}{D(\underline{\xi})}\right)d\theta d\zeta_3 \tag{D.12}$$

This expression has been numerically integrated with the method of Gauss–Legendre quadrature (order $n = 100$):

$$S_{ijmn} = \sum_k^{N_k}\sum_l^{N_l} w_k w_l f(p_k, (1+p_l)\pi) \quad (0 < w < 1, -1 < p < 1) \tag{D.13}$$

For the infinite cylinder inclusion, which corresponds to the DS microstructure, a_3 is taken to 10^6, which is huge in front of $a_1 = a_2 = 1$.

References

Alexandre, F., Deyber, S., Pineau, A., 2004. Modelling the optimum grain size on the low cycle fatigue life of a ni based superalloy in the presence of two possible crack initiation sites. Scr. Mater. 50, 25–30.

Bernhardi, O., Mücke, R., 2000. A lifetime prediction procedure for anisotropic materials. Commun. Numer. Methods Eng. 16, 519–527.

Berveiller, M., Zaoui, A., 1979. An extension of the self-consistent scheme to plastically flowing polycrystal. J. Mech. Phys. Solids 26, 325–344.

Cailletaud, G., 1992. A micromechanical approach to inelastic behaviour of metals. Int. J. Plast. 8, 55–73.

Cailletaud, G., Saï, K., 2008. A polycrystalline model for the description of ratchetting: effect of intergranular and intragranular hardening. Mater. Sci. Eng. A 480, 24–39.

Chen, L., Wen, W., Cui, H., 2012. Yielding description for a Ni3Al based intermetallic alloy. Mater. Des. 41, 192–197.

Chu, Z., Yu, J., Sun, X., Guan, H., Hu, Z., 2010. Tensile property and deformation behavior of a directionally solidified Ni-base superalloy. Mater. Sci. Eng. A 527, 3010–3014.

Eshelby, J., 1957. The determination of the elastic field of an ellipsoidal inclusion, and related problems. Proc. R. Soc. London 241, 376–396.

Gordon, A.P., Neu, R.W., McDowell, D.L., 2009. Effect of pre-exposure on crack initiation life of a directionally solidified Ni-base superalloy. Int. J. Fatigue 31, 393–401.

Gordon, A.P., Trexler, M.D., Neu, R.W., Sanders Jr., T.J, McDowell, D.L., 2007. Corrosion kinetics of a directionally solidified ni-base superalloy. Acta Mater. 55, 3375–3385.

Han, S., Li, S., Smith, D.J., 2001a. Comparison of phenomenological and crystallographic models for single crystal nickel base superalloys. I. Analytical identification. Mech. Mater. 33, 251–266.

Han, S., Li, S., Smith, D.J., 2001b. Comparison of phenomenological and crystallographic models for single crystal nickel base superalloys. II. Numerical simulations. Mech. Mater. 33, 267–282.

Hanriot, F., Cailletaud, G., Rémy, L., 1991. Mechanical behaviour of a nickel-base superalloy single crystal. In: Freed, A., Walker, K. (Eds.), Proc. of Int. Symp. High Temperature Constitutive Modeling: Theory and Application, Atlanta, Georgia, Winter Annual Meeting. ASME.

Hasebe, T., Sakane, M., Ohnami, M., 1992. Elastic anisotropy of directionally solidified superalloy. J. Eng. Mater. Technol. 114, 141–146.

Hendrix, B., Yu, L., 1998. Self-consistent elastic properties for transversely isotropic polycrystals. Acta Mater. 46, 127–135.

Hill, R., 1965. Continuum micro-mechanisms of elastoplastic polycrystals. J. Mech. Phys. Solids 13, 89–101.

Ibanez, A., Srinivasan, V., Saxena, A., 2006. Creep deformation and rupture behaviour of directionally solidified GTD 111 superalloy. Fatigue Fract. Eng. Mater. Struct. 29, 1010–1020.

Kneer, G., 1965. Über die Berechnung der Elastizitätsmoduln Vielkristalliner Aggregate mit Textur. Phys. Status Solidi B 9, 825–838.

Kowalewski, R., Mughrabi, H., 1998. Influence of a plasma-sprayed NiCrAlY coating on the low-cycle fatigue behaviour of a directionally solidified nickel-base superalloy. Mater. Sci. Eng. A 247, 295–299.
Kröner, E., 1961. Zur plastischen Verformung des Vielkristalls. Acta Metall. 9, 155–161.
Kupkovits, R., Neu, R., 2010. Thermomechanical fatigue of a directionally-solidified Ni-base superalloy: smooth and cylindrically-notched specimens. Int. J. Fatigue 32, 1330–1342.
Latief, F., Kakehi, K., Yeh, H.A.-C., Murakami, H., 2014. Influences of ruthenium and crystallographic orientation on creep behavior of aluminized nickel-base single crystal superalloys. Mater. Sci. Eng. A 592, 143–152.
Moore, Z., Neu, R., 2011. Creep fatigue of a directionally solidified Ni-base superalloy: smooth and cylindrically notched specimens. Fatigue Fract. Eng. Mater. Struct. 34, 17–31.
Mura, T., 1987. Micromechanics of Defects in Solids. Martinus Nijhoff.
Nie, J., Liu, Z., Liu, X., Zhuang, Z., 2009. Size effects of γ' precipitate on the creep properties of directionally solidified nickel-base super-alloys at middle temperature. Comput. Mater. Sci. 46, 400–406.
Okada, M., Tsutsumi, M., Kitamura, T., Hohtani, R., 1998. Initiation and growth of small cracks in directionally solidified MAR-M247 under creep-fatigue. Part I: effect of microstructure. Fatigue Fract. Eng. Mater. Struct. 21, 741–750.
Österle, W., Bettge, D., Fedelich, B., Klingelhöffer, H., 2000. Modelling the orientation and direction dependence of the critical resolved shear stress of nickel-base superalloy single crystals. Acta Mater. 48, 689–700.
Paquin, A., Berbenni, S., Favier, V., Lemoine, X., Berveiller, M., 2001. Micromechanical modelling of the elastic-viscoplastic behavior of pollycrystalline steels. Int. J. Plast. 17, 1267–1302.
Pilvin, P. 1994. The contribution of micromechanical approaches to the modelling of inelastic behaviour. In: Pineau, A., Cailletaud, G., Lindley, T. (Eds), Fourth Int. Conf. on Biaxial/Multiaxial Fatigue, Saint-Germain, France, ESIS, vol. 1, pp. 31–46.
Prasad, S.C., Rajagopal, K., Rao, I., 2006. A continuum model for the anisotropic creep of single crystal nickel-based superalloys. Acta Mater. 54, 1487–1500.
Prasad, S.C., Rao, I., Rajagopal, K., 2005. A continuum model for the creep of single crystal nickel-base superalloys. Acta Mater. 53, 669–679.
Sabar, H., Berveiller, M., Favier, V., Berbenni, S., 2002. A new class of micro–macro models for elastic–viscoplastic heterogeneous materials. Int. J. Solids Struct. 39, 3257–3276.
Saï, K., Cailletaud, G., Forest, S., 2006. Micro-mechanical modeling of the inelastic behavior of directionally solidified materials. Mech. Mater. 38, 203–217.
Shenoy, M., McDowell, D., Neu, R., 2006. Transversely isotropic viscoplasticity model for a directionally solidified Ni-base superalloy. Int. J. Plast. 22, 2301–2326.
Shi, D., Dong, C., Yang, X., 2013. Constitutive modeling and failure mechanisms of anisotropic tensile and creep behaviors of nickel-base directionally solidified superalloy. Mater. Des. 45, 663–673.
Shi, D., Dong, C., Yang, X., Zhang, L., Hou, J., Liu, Y., 2012. Experimental investigations on creep rupture strength and failure mechanism of vacuum brazed joints of a DS superalloy at elevated temperature. Mater. Sci. Eng. A 545, 162–167.
Shi, D., Liu, J., Yang, X., Qi, H., Wang, J., 2010. Experimental investigation on low cycle fatigue and creep-fatigue interaction of DZ125 in different dwell time at elevated temperatures. Mater. Sci. Eng. A 528, 233–238.
Stewart, C.M., Gordon, A.P., Ma, Y.W., Neu, R.W., 2011. An anisotropic tertiary creep damage constitutive model for anisotropic materials. Int. J. Press. Vessels Pip. 88, 356–364.
Suvorov, A., Dvorak, G., 2002. Rate form of the Eshelby and Hill tensors. Int. J. Solids Struct. 39, 5659–5678.
Transvalor and ENSMP. 2010. ZéBuLon 8.4.4 References Manuals. Northwest Numerics.
Vladimirov, I.N., Reese, S., Eggeler, G., 2009. Constitutive modelling of the anisotropic creep behaviour of nickel-base single crystal superalloys. Int. J. Mech. Sci. 51, 305–313.
Wang, L., Xie, G., Zhang, J., Lou, L., 2006. On the role of carbides during the recrystallization of a directionally solidified nickel-base superalloy. Scr. Mater. 55, 457–460.
Xia, P., Yu, J., Sun, X., Guan, H., Hu, Z., 2008. Influence of γ' precipitate morphology on the creep property of a directionally solidified nickel-base superalloy. Mater. Sci. Eng. A 476, 39–45.
Yaguchi, M., Busso, E., 2005. On the accuracy of self-consistent elasticity formulations for directionally solidified polycrystal aggregates. Int. J. Solids Struct. 42, 1073–1089.
Yaguchi, M., Yamamoto, M., Ogata, T., Ohno, N., 2007. An anisotropic constitutive model for a directionally solidified superalloy. Key Eng. Mater. 340–34, 901–906.
Yamamoto, M., Kitamura, T., Ogata, T., 2008. Influence of microscopically distributed inhomogeneity and anisotropy of grains on high-temperature crack propagation properties of directionally solidified superalloy. Eng. Fract. Mech. 75, 779–789.
Yang, X., Dong, C., Shi, D., Zhang, L., 2011. Experimental investigation on both low cycle fatigue and fracture behavior of DZ125 base metal and the brazed joint at elevated temperature. Mater. Sci. Eng. A 528, 7005–7011.
Yuan, C., Guo, J., Yang, H., Wang, S., 1998. Deformation mechanism for high temperature creep of a directionally solidified nickel-base superalloy. Scr. Mater. 39, 991–997.
Zhao, Y., Wang, L., LI, H., Yu, T., Liu, Y., 2008. Effects of recrystallization on the low cycle fatigue behavior of directionally solidified superalloy DZ40M. Rare Met. 27, 425–428.